1
2
3
4
5
6
7
8
9
10
11
12
13
14
15
16
17
18
19
20
21
22
23
24
25
26
27
28
29
30
31
32
33
34
35
36
37
38
39
40
41
42
43
44
45
46
47
48
49
50
51
52
53
54
55
56
57
58
59
60

Analysis of ethyl and methyl centralite vibrational spectra for mapping organic gunshot residues

Jianbo Zeng,[a] Ji Qi,[a] Fuquan Bai,[b] Jorn Chi Chung Yu,[c] Wei-Chuan Shih[a*]

AUTHOR ADDRESS

[a]Department of Electrical and Computer Engineering, University of Houston, 4800 Calhoun Road, Houston, TX 77204-4005, USA

[b]State Key Laboratory of Theoretical and Computational Chemistry, Institute of Theoretical Chemistry, Jilin University, Changchun, 130023, People's Republic of China

[c]College of Criminal Justice, Sam Houston State University, Box 2525, 1003 Bowers Blvd., Huntsville, TX 77341, USA

[*]Corresponding Author, Email: wshih@uh.edu Phone: +1 713-743-4454; Fax: 713-743-4444

1

Abstract

Detection of ethyl and methyl centralites in gunshot residues is important in forensic science due to their limit contamination from environmental sources compared to other organic residues. However, the vibrational frequencies of centralites are little explored and their frequency assignments are incomplete. Herein, we investigated vibrational frequencies of centralites based on Density Functional Theory (DFT) to understand their vibrations. The simulated frequencies exhibit an excellent agreement with the experimental data, and the detail assignments are comprehensively elaborated. We also demonstrate that centralite particles could be detected through Raman imaging based on their fingerprints. This work is very important for the further vibrational studies in detecting and tracing centralites in gunshot residues.

Keywords: forensic science, criminalistics, centralites, Raman imaging, vibrational spectra, organic gunshot residues.

Introduction

Gunshot residues (GSR) are a mixture of burnt, partially burnt and unburnt byproducts consisting of inorganic particles and organic compounds as two major classes of constituents. There are two common types of GSR in forensic trace evidence examination. The first type is the GSR deposited around the area of target. Most of these GSR originated from the materials in the barrel of a gun mixed with burned, unburned, or partially burned gunpowder, therefore, contains metal particulates, such as lead, copper, brass, or nickel from jacketing material. This type of GSR is useful for the determination of the shooting distance, which is the distance between the muzzle of a gun and a target. The second type of GSR is collected from the hands or clothing of a suspected shooter. This type of GSR is commonly known as primer GSR. A particle must meet certain criteria such as size and shape to become recognized as primer GSR.[1]

Primer GSR analysis is of great interest to forensic scientists due to its potential use in criminal justice to provide evidence of whether a suspect discharged a firearm.[2,3,4] State-of-the-art GSR analysis is primarily based on detecting "GSR particles", also known as primer GSR microparticles consisting of elemental lead, barium and tin, using scanning electron microscopy coupled with energy dispersive X-ray spectroscopy (SEM/EDX).[4] Because the identification of primer GSR heavily relies on the experience of the GSR analyst, the current technique has been subjective and often plagued by false negatives due to the lack of detected primer particles in the

collected samples. Further, it is well recognized that SEM/EDX may not provide convincing specificity for alternative primer materials such as Bismuth (Bi) and glass that are commonly found in domestic products and materials. Therefore, there is a critical need to significantly broaden the current GSR analysis by considering other inorganic as well as organic substances. However, to detect other inorganic or organic substances requires the unavoidable destruction of samples as they are processed to extract molecular composition, e.g., gas chromatography, thereby compromising potentially valuable evidence. Besides, due to the matrix effect and sophisticated sample preparation steps, there may not be enough quantity for current chromatography based techniques to provide accurate and robust answers. Further, these existing analytical techniques, e.g., SEM/EDX, gas chromatography (GC), atomic absorbance spectroscopy (AAS), and inductively coupled plasma atomic emission spectroscopy (ICP/AES), typically involve highly skilled personnel labor, expensive equipment and dedicated laboratory space.

To broaden the current GSR analysis repertoire, alternative GSR consisting of organic molecules such as nitrocellulose and common stabilizer such as diphenylamine, centralites, and resorcinol have been analyzed by high performance liquid chromatography (HPLC), mass spectrometry, and vibrational spectroscopy.[2,5,6] Among these organic compounds, ethyl centralite (EC) and methyl centralite (MC) have been considered as signature compounds for GSR, including gunpowder and primer residues.[7] MC and EC are good indicators in demonstrating the presence of GSR because they are highly specific to smokeless powders with very few significant

4

environmental sources; whereas, the stabilizer diphenylamine, in addition to ammunitions, has known industrial and agricultural uses. Thus, centralites could become an alternative identifier that is presumably exclusive enough to smokeless powders so as to prevent false outcomes.[8] Various techniques, including HPLC,[9,10] fluorescence,[11] desorption electrospray ionization (DESI)-tandem mass spectrometry,[12] and Raman spectroscopy,[13] have been applied to analyze centralites. Compared to other techniques, vibrational spectroscopy including Raman scattering and infrared (IR) absorption spectroscopy, provide rich vibrational "fingerprinting" information directly related to chemical bonds and molecular configurations, enabling fast and robust identification of the organic compounds. In addition, vibrational techniques rely on light-matter interactions, which is non-invasive and require minimal or no sample preparation. Thus, the integrity of key forensic evidence can be retained.

There have been a growing number of research focusing on analyzing GSR by Raman and IR spectroscopy and imaging,[5,6,14,15,16] which are often coupled with chemometrics.[5,15] Moreover, the spectroscopic imaging based on the vibrational frequency is an alternative technique in analyzing GSR because of its rich fingerprint vibrations and fast and non-destructive detections.[16] It can overcome the disadvantages of SEM/EDS as mentioned earlier. Although the Raman spectrum of EC had been recorded,[13] a comprehensive vibrational band assignment is not available. The incomplete vibrational landscape of centralites could hinder further research and development of potentially transformative techniques. Therefore, it is

essential to investigate the vibrational landscape of centralites using both simulation and experimental techniques. Density functional theory (DFT) is an excellent method to simulate vibrational frequencies from the first principle due to its excellent performance in calculating both ground state properties and potential energies.[17] With the aid of DFT, detailed vibrational landscape of centralites can be comprehensively determined and compared with experimental results.

In this work, EC and MC's geometrical structures were optimized through Lee-Yang-Parr correlation functional (B3LYP), and the vibrational spectra are simulated by B3LYP/6-311++g(df,pd) method. The simulated frequencies, accompanied with agreeing experimental results, provide comprehensive Raman and IR band assignments for the first time. We further demonstrate that high-throughput line-scan Raman microscopy (LSRM) is a powerful tool to analyze EC and MC based on their Raman spectra. The results presented here would lay the groundwork for further vibrational studies of centralites, as well as technology development.

Experimental

EC and MC were purchased from Sigma-Aldrich (St. Louis, MO, USA). The IR spectra were obtained using a Perkin-Elmer Spectrum One spectrometer with an attenuated total reflectance (ATR) accessory. The Raman spectra of centralite powders were recorded by a home-built line-scan Raman microscope (LSRM) as described in our previous paper.[18] Briefly, the LSRM employs the 785 nm output of a continuous wave (CW) titanium:sapphire laser (Spectra-Physics 3900S) pumped by a

532 nm diode-pumped solid state laser (Spectra-Physics Millennia 10X). The 785 nm

laser was projected onto the sample as a line, from which the Raman scattered

photons were collected and imaged to the entrance slit of a dispersive spectrograph

(Princeton LS785) and recorded by a charge coupled device (CCD) camera (Princeton

PIXIS 400BR).

The DFT calculations were performed using GAUSSIAN 09[19] program package

on a INSPUR computer system. The fully optimal molecular structures of EC and MC

were obtained based on the hybrid of Beckes nonlocal three parameter exchange and

correlation functional and Lee-Yang-Parr correlation functional (B3LYP).[20,21] Thus,

the vibrational frequencies of centralites were calculated at the DFT (B3LYP) levels

of theory using the 6-31++G(2d,p) basis set. The experimental spectra were compared

to the simulated spectra to make vibrational normal mode assignments. The detail

band assignments were determined by inspection of the Gaussview representations of

the normal modes, and the corresponding vibration was observed in the molecular

model.

7

Results and discussion

(a)   (b)

(c)   (d)
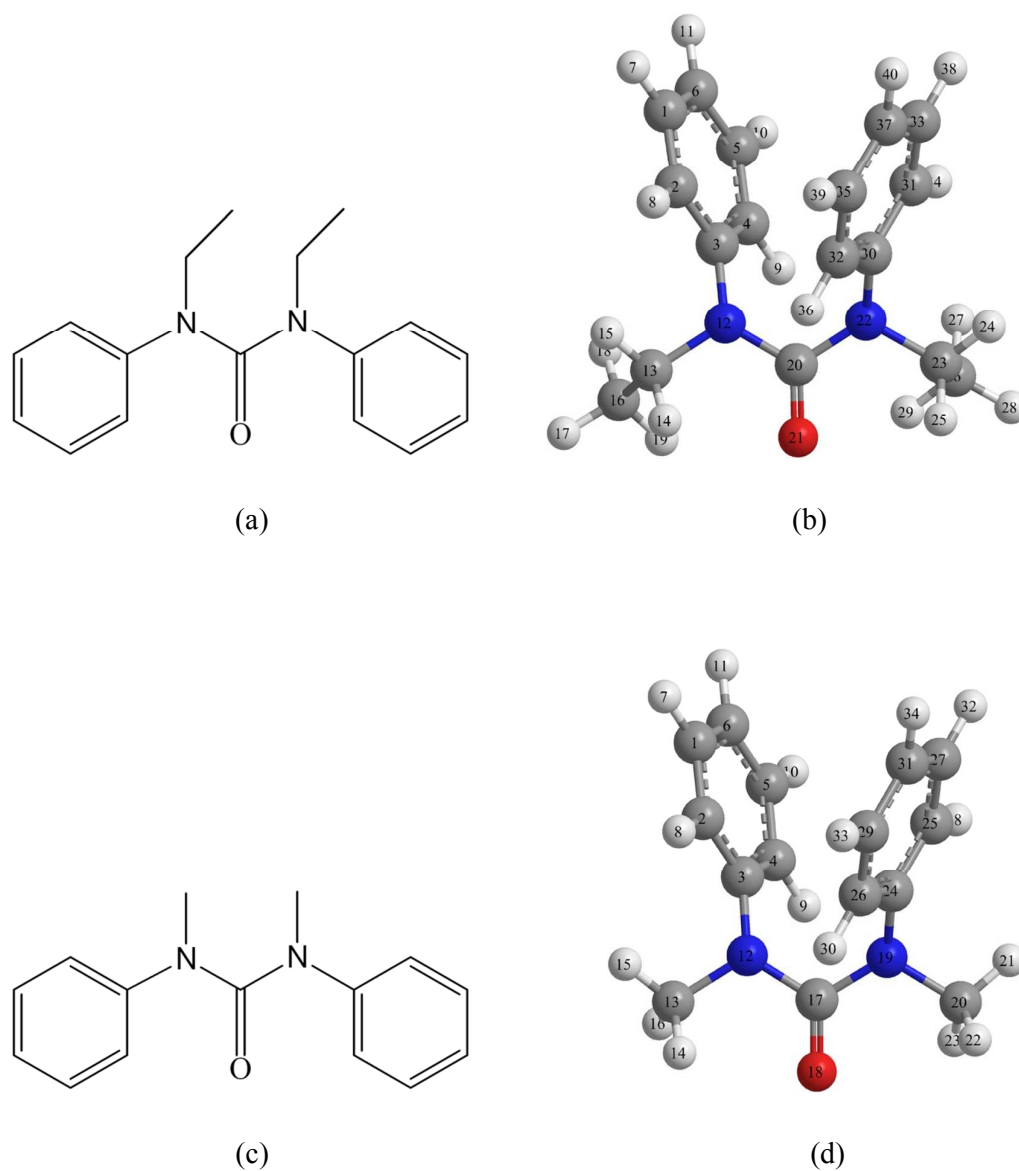
Figure 1 The structural formula of EC (a) and MC (c) and the corresponding optimized geometrical structures of EC (b) and MC (d), which are calculated by DFT with B3LYP/6-311++g(df,pd) through GAUSSIAN 09. Blue: nitrogen; Red: oxygen; Dark grey: carbon; Ligh tgrey: hydrogen.

Geometrical structure EC and MC were first simulated by DFT methods to

investigate the molecular structures, as well as the vibrational spectra. Figure 1a and c

demonstrate the structural formula of EC and MC, respectively, and their calculated

geometrical structures (Figure 1b and d) fully optimized by Lee-Yang-Parr correlation

functional (B3LYP). As shown in Figure 1, the C-N freely rotating single-bonds

significantly affect the molecular geometries of EC and MC. The obtained

geometrical parameters of EC and MC, including bond lengths and bond angles, are

presented in Table 1. For EC, the N12-C20 length is shortened by 0.085 and 0.040 Å

compared to the N12-C13 and N12-C3 lengths, respectively. Similarly, the N22-C20

also exhibits a shorter length. The C20-O21 length of the carbonyl group is 1.224 Å

which is shorter compared with those of N12-C20 (1.389 Å) and C20-N22 (1.395 Å)

due to the large polarity of the carbon oxygen double bonds. The N12-C20-N22 angle

is found to be 116.6°, and it is about 5.2° and 5.0° smaller than those of N12-C20-O21

and N22-C20-O21, respectively. In addition, the C3-N12-C20 (123.4°) and

C20-N12-C30 (122.0°) with large angles over that of N12-C20-N22 distort the

parallel structure of two face-to-face benzene rings and result in a slightly opened

geometrical structure. In comparison to the C3-N12-C20 angle, the angles of

C3-N12-C13 (117.1°) and C13-N12-C20 (116.6°) are also small. The C20-N22-C23

and C23-N22-C30 angles exhibit the same behavior. MC has a structure similar to EC

except the ethyl group, and its optimized geometrical structure is quite similar. As can

be seen in Table 1, the bond lengths and bond angles have small discrepancies, and

most of them are quite similar.

9

Table 1 Bond length and bond angles of EC and MC optimized by B3LYP

EC		MC	
Bond length (Å)		Bond length (Å)	
C1-C2	1.390	C1-C2	1.390
C1-C6	1.391	C1-C6	1.392
C2-C3	1.395	C2-C3	1.394
C3-C4	1.396	C3-C4	1.395
C3-N12	1.429	C3-N12	1.431
C4-C5	1.390	C4-C5	1.390
C4-C9	1.082	C4-C9	1.083
C5-C6	1.391	C5-C6	1.391
N12-C13	1.474	N12-C13	1.466
N12-C20	1.389	N12-C17	1.391
C13-C16	1.527		
C20-O21	1.224	C17-O18	1.222
C20-N22	1.395	C17-N19	1.391
N22-C23	1.479	N19-C20	1.466
N22-C30	1.428	N19-C24	1.431
C23-C26	1.525		
C30-C31	1.395	C24-C25	1.394
C30-C32	1.396	C24-C26	1.395
C31-C33	1.390	C25-C27	1.390
C32-C35	1.390	C26-C29	1.390
C33-C37	1.391	C27-C31	1.392
C35-C37	1.391	C29-C31	1.391
Bond angle (°)		Bond angle (°)	
C2-C1-C6	120.3	C2-C1-C6	120.3
C1-C2-C3	120.4	C1-C2-C3	120.3
C2-C3-C4	119.2	C2-C3-C4	119.4
C2-C3-N12	120.0	C2-C3-N12	119.8
C4-C3-N12	120.8	C4-C3-N12	120.8
C3-C4-C5	120.3	C3-C4-C5	120.2
C4-C5-C6	120.3	C4-C5-C6	120.3
C4-C5-C10	119.6	C4-C5-C10	119.6
C6-C5-C10	120.1	C6-C5-C10	120.1
C1-C6-C5	119.5	C1-C6-C5	119.6
C3-N12-C13	117.1	C3-N12-C13	116.2
C3-N12-C20	123.4	C3-N12-C17	122.4
C13-N12-C20	116.6	C13-N12-C17	115.8
N12-C13-C16	113.9	N12-C13-H14	109.4
N12-C13-H14	107.1	N12-C13-H15	108.8
N12-C13-H15	107.3	N12-C13-H16	111.7
N12-C20-O21	121.8	N12-C17-O18	121.8

10

N12-C20-N22	116.6	N12-C17-N19	116.3
O21-C20-N22	121.6	O18-C17-N19	121.8
C20-N22-C23	115.8	C17-N19-C20	115.8
C20-N22-C30	122.0	C17-N19-C24	122.4
C23-N22-C30	117.1	C20-N19-C24	116.2
N22-C23-C26	113.3	N19-C20-H21	108.9
N22-C23-C24	106.6	N19-C20-H22	111.7
N22-C23-C25	108.8	N19-C20-H23	109.4
N22-C30-C31	119.9		
N22-C30-C32	120.9	N19-C24-C25	119.8
C31-C30-C32	119.2	N19-C24-C26	120.8
C30-C31-C33	120.4	C25-C24-C26	119.4
C30-C32-C35	120.3	C24-C25-C27	120.3
C31-C33-C37	120.3	C24-C26-C29	120.2
C37-C33-C38	120.1	C25-C27-C31	120.3
C37-C35-C37	120.4	C26-C29-C31	120.3
C33-C37-C35	119.5	C27-C31-C29	119.6

Vibrational spectra and band assignments Theoretical Raman and IR frequencies of EC and MC, as well as their intensities, were calculated from the B3LYP using the extended 6-311++g(df,pd) basis set. Experimental Raman and IR spectra of powers were obtained to better identify the frequencies. The frequencies of the CH vibrations above 2500 cm^{-1} was scaled by a factor of 0.960 derived from the reported scaling factor for the valence A-H stretching force constants, while the harmonic frequencies below 2000 cm^{-1} were scaled by a factor of 0.982.[22] For comparisons, Figure 2 and 3 show theoretical/experimental Raman and IR spectra of EC, respectively. The corresponding assignments of Raman and IR frequencies were summarized in Table 2. Moreover, the spectral characteristics of MC are shown in Fig. 4 and 5, and the vibrational assignments are detailed in Table 3.   Good agreement has been observed from both theoretical frequencies and experimental observed results.

11
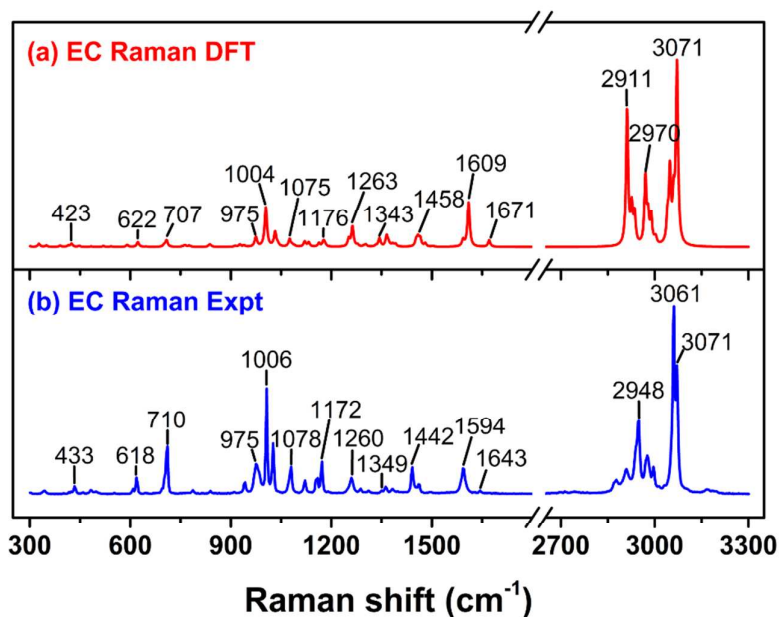
Figure 2 Raman spectra of ethyl centralite (1,3-diethyl-1,3-diphenylurea): (a) theoretical calculation based on DFT and (b) Raman spectrum obtained using 785 nm laser excitation.
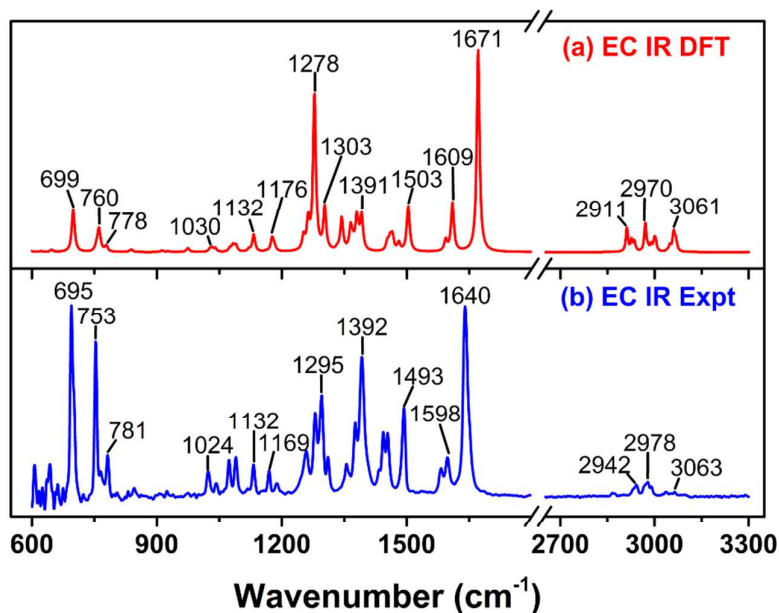
Figure 3 IR spectra of ethyl centralite (1,3-diethyl-1,3-diphenylurea): (a) theoretical calculation based on DFT and (b) IR spectrum obtained using ATR-IR.

12

C=O vibrations of EC The carbonyl group as a covalent C=O double bond comprised

of a carbon atom double-bonded to an oxygen atom is an important functional group

in a large number of different classes of compounds such as ketones and carboxyl

acids etc. As a strongly polarized asymmetric chemical bond, it exhibits intense

absorption feature in the region 1600-1800 cm^{-1} in IR spectra.[23] Thus, it is a most

characteristic to identify organic compounds. The complementary Raman band

provides much weaker intensity in this region. Figure 2a and b display the simulated

and experimental Raman frequencies of EC, respectively. The C=O stretching appears

at 1643 cm^{-1} (Fig. 2b), while the simulated frequency (Fig. 2a) is at 1671 cm^{-1} that is

mostly overestimated by 28 cm^{-1}. However, its weak intensity predicted by the

simulation is consistent with the experimental observation. As expected in IR spectra

(Fig. 3a and b), the C=O stretching demonstrates very strong IR absorption around

1640 cm^{-1} which dominates the whole spectra. Both simulated and experimental

frequencies of EC C=O stretching are consistent with those of 1,3-diphenylurea that

was recently reported by Badawi and coworkers.[24] It is noted that smokeless

gunpowders contain some common components such as nitrocellulose, nitroglycerin

and dinitrotoluene which exhibit an intense IR band at ~1650 cm^{-1} attributed to the

antisymmetric NO_2 stretching.[14] Thus, this strong band will overlap with that of the

C=O stretching mode, and limits the analysis of EC based on the C=O stretching in IR

spectra. According to the simulated results, the C=O in-plane bending associated with

other vibrational modes contributes to a few frequencies of Raman (or IR) spectra in

low frequencies, including 400, 643 and 839 cm^{-1} (Fig. 2a). However, their intensities

are quite weak in both Raman and IR spectra.

C-N, C-N-C, and N-C-N vibrations of EC The nitrogen atom together with the

carbonyl group in the EC molecular structure is an important functional group, and

the carbon-nitrogen bond is considered as one of the most abundant covalent bonds.

The associated vibrational modes, including C-N, C-N-C, and N-C-N vibrations,

would provide rich information for characterizing the compound. According to the

simulated results (Fig. 2a and 3a), the C-N stretching of C3-N12, C13-N12, C23-N22,

and C30-N22 significantly contributes to the frequencies at 1121, 1176, 1252 and

1263 cm^{-1} in the spectral region from 1100 to 1300 cm^{-1}. The observed frequencies at

1503 and 1609 cm^{-1} with a moderate intensity also involves contribution from the

C3-N12 and C30-N22 stretching. However, the out-of-plane bending of C3-N12 and

C23-N22 appears at the low wavenumbers in Raman spectra. The comprehensive

frequency assignments are listed in Table 2. For C-N-C vibrations, two frequencies at

1365 and 1343 cm^{-1} are primarily attributed to the asymmetrical stretching of

C3-N12-C20 and C20-N22-C30, respectively. The C13-N12-C20 scissoring is

observed at 423 cm^{-1} in Raman spectra. The N12-C20-N22 symmetrical stretching

shows up at 975 cm^{-1} coupled with ring breathing and H-C-H twisting. It has a

moderate intensity in Raman spectra, while its intensity in IR spectra is extremely

weak. The N12-C20-N22 asymmetrical stretching associated with the C-N stretching

and the C-C-C asymmetrical stretching results an intense IR frequency at 1278 cm^{-1}.

However, it is relatively weak in Raman spectra. According previous reports,[5,14]

14

nitrocellulose also exhibits a strong frequency at 1275~1287 cm^{-1} due to the symmetric NO$_2$ stretching. Our simulated results provide detail assignments for both IR and Raman frequencies of EC in this spectral region. It is helpful to identify EC in GSR.

Phenyl ring vibrations of EC As shown in Fig. 1a, there are two phenyl rings attached to the nitrogen atoms in the EC molecular structure. We assigned the phenyl ring having carbon atoms from C1 to C6 as ring 1, and the other one with carbon atoms from C30 to C37 as ring 2. The phenyl ring spectral region predominantly involves various vibrational modes, including ring breathing, ring bending, C-H stretching, C-C-C symmetrical and asymmetrical stretching. In the experimental Raman spectrum (Fig. 2b), the ring breathing exhibits an intense peak at 1006 cm^{-1}, which is considered as an important characteristic for phenyl ring vibrations in the fingerprint region. It is in very good agreement with the simulated frequency at 1004 cm^{-1} (Fig. 2a). Louden and coworkers successfully determined the penetration depth and concentration profile in the methyl centralite/nitrocellulose by using the relative frequency intensity measurement of centralite phenyl ring breathing and nitrocellulose NO$_2$ deformation.[25] According to the simulated results, the ring breathing couples with other vibrational modes also the frequencies at 974, 944 and 913 cm^{-1} (Table 2). The phenyl ring bending is observed at the low wavenumber regions blow 750 cm^{-1} e.g. the out-of-plane bending at 552, 608, 695 and 710 cm^{-1}, and the in-plane bending at 648, 618, 459 and 433 cm^{-1}.

The frequencies originating from the ring C-H stretching of EC was observed in the spectral region from 3000 to 3100 cm^{-1}. It agrees with previous reports of the ring C-H-stretching vibrations.[26,27] In Raman spectra (Fig. 2), the ring C-H stretching at 3061 and 3071 cm^{-1} exhibits a very strong intensity. The frequency at 3061 cm^{-1} involves two parts of the C-H stretching modes that are from the C2-H8, C4-H9, C4-H9 and C6-H11 stretching of ring 1, and the C31-H34, C32-H36, C33-H38 and C37-H40 stretching of ring 2. The frequency at 3071 cm^{-1} are assigned to all the C-H stretching modes of both rings. Those vibrations are very weak in IR spectra. Most importantly, the simulated Raman and IR spectra match with the experimental Raman and IR spectra, respectively.

The ring C-C-C symmetrical and asymmetrical stretching primarily contributes to the frequencies at ~1030, ~1300, ~1500 and ~1600 cm^{-1}. According to the simulated frequencies, the frequency at 1032 cm^{-1} is due to the C1-C6-C5 and C33-C37-C35 symmetrical stretching, while the ring C-C-C asymmetrical stretching significantly dominates the frequencies at ~1300, ~1500 and ~1600 cm^{-1} (Table 2).

Table 2 The experimental and calculated IR and Raman spectra of ethyl centralite.

Mode	Raman		IR		Assignments
	Expt	DFT	Expt	DFT	
17		327			*β*ring2, *τ*(C23-C26), *τ*(C13-C16)
18	342	349			*τ*(C13-C16), *τ*(C23-C26), *γ*(C23-N22), *β*ring1, *β*ring2
19	400	390			*β*(C20=O21), *γ*(C23-N22), *τ*(C13-C16), *τ*(C23-C26)
20	416	414			*τ* ring2, *τ* ring1,
22	433	424			*ciss*(N12–C20=O21), *ciss*(C13-N12-C20), *β* ring1
23	459	448			*γ*(C3-N12), *β*ring1
24	482	482			*τ* ring1, *τ* ring2, *γ*(C13–N12)
25	498	520			*γ*(C23-N22), *γ*(C30–N22), *γ*ring2
26	552	543			*γ*ring2, *γ*ring1, *γ*(C3-N12)

27	608	590			γring1, γring2, *ciss*(N12-C20-N22)
28	618	623	616	621	βring1, βring2
30	643	648	642	651	β(C20=O21), βring1, βring2,
32	695	700	696	700	γring1, γring2,
33	710	707			γring1, γring2,
36		763	753	756	γ(C33-H38),γ(C35-H39), γ(C37-H40), rock(H24-C23-H25), rock(H14-C13-H15)
37	786	776	776	778	γ(C1-H7),γ(C5-H10), γ(C6-H11)
41	839	837	830	834	β(C20=O21), β(CH$_3$)
43	909	913	915	913	γ(C2-H8),γ(C4-H9), γ(C6-H11), ν(C13-C16), ring1 breathing
45	941	939	948	944	ν(C23-C26), ring2 breathing, γ(C31-H34),γ(C32-H36), γ(C37-H40)
48	976	975	970	975	ν(N12–C20-N22), ring(1,2) breathing, *twist*(H14-C13-H15), *twist*(H24-C23-H25),
					ring (1,2) breathing
52	1006	1004			ν_s(C1-C6-C5, C33-C37-C35)
54	1026	1032	1024	1032	ν_{as}(N12-C14-C16, N22-C25-C26), β(C-H) in ring (1,2)
55			1043	1040	*wag*(H18-C16-H19, H27-C26-H29), ν(C23-C26, C13-C16)
56	1078	1075	1073	1075	ν(C-C) in ring, *umbrella*(C16-H$_3$, C26-H$_3$)
57		1083	1088	1083	ν(C13-N12, C23-N22), rock(H14-C13-H15, H24-C23-H25),
60	1121	1121	1122	1123	*wag*(H17-C-H19, H28-C26-H29)
61		1132	1132	1132	*rock*(H14-C13-H15, H24-C23-H25), *wag*(H17-C-H19, H28-C26-H29),
					ν_{as}(N12-C20-N22)
63	1155	1163			β(C5-H11, C1-H7, C5-H10, C2-H8), β(C37-H40)
64	1172	1176	1177	1178	ν(C13-N12, C23-N22), β(C5-H10, C2-H8, C4-H9, C31-H34, 31-H34, C32-H35,
					C35-H39)
67		1252	1258	1252	*twist*(H14-C13-H15, H24-C23-H25), ν(C3-N12, C30-N22)
68	1259	1263	1280	1263	ν(C3-N12, C30-N22), *twist*(H14-C13-H15, H24-C23-H25)
69	1287	1278	1295	1278	ν_{as}(N12-C20-N22), ν(C13-N12, N22-C23), ν_{as}(C2-C3-C4, C31-C30-C32)
71	1310	1303	1311	1303	ν_{as}(C-C-C) in rings, ν_{as}(N12-C20-N22)
74	1349	1343	1355	1343	ν_{as}(C20-N22-C30),*wag*(H24-C23-H25)
75	1360	1365			ν_{as}(C3-N12-C20), *wag*(H14-C13-H15), *wag*(H24-C23-H25)
78	1381	1382	1376	1379	ν(C13-C16), ν(C23-C26)
79	1397	1392	1392	1391	ν_{as}(N12-C20-N22), ν(C23-C26), *wag*(H14-C13-H15, H24-C23-H25), *umbrella*
					(C26-H$_3$)
82	1442	1458	1443	1462	*sciss*(H24-C23-H25, H27-C25-H28), ν_{as}(C-C-C) in rings
87	1462	1480	1454	1480	*sciss*(H27-C26-H29, H28-C26-H29)
89	1497	1503	1493	1503	ν_{as}(C-C-C) in rings, ν(C3-N12, C30-N22)
90	1587	1592	1581	1592	ν_{as}(C2-C3-C4, C1-C6-C5, C31-C30-C32, C33-C37-C35)
93	1594	1609	1598	1609	ν_{as}(C-C-C) in rings, ν_s(C-C-C) in rings, ν(C3-N12, C30-N22)
94	1643	1671	1640	1671	ν(C20=O21), *sciss*(H14-C13-H15, H24-C23-H25)
96	2876	2911	2865	2911	ν(C16-H17, C16-H18, C16-19)
97	2908	2926			ν_s(H24-C23-H25)
100	2948	2970	2942	2970	ν_{as}(H27-C26-H28), ν(C23-H24)
101	2976	2978			ν_{as}(H28-C26-H29), ν_{as}(H24-C23-H25)
102	2996	2988	2978	2988	ν_{as}(H17-C16-H19), ν(C13-H14)
104	3014	3003	2990	3000	ν_{as}(H14-C13-H15, H18-C16-H19)

17

107	3048	3048	3054	3048	ν(C1-H7, C2-H8, C4-H9, C5-H10, C31-H34, C32-H36, C33-H38, C35-H39)
110	3061	3061	3063	3061	ν(C2-H8, C4-H9, C4-H9, C6-H11, C31-H34, C32-H36, C37-H40)
114	3071	3071			ν(C-H) in rings

Abbreviations: ν, stretching; β, in-plane bending; γ, out-of-plane bending; τ, torsional vibration; sciss, scissoring; rock, rocking; wag, wagging; twist, twisting; ν_s, symmetrical stretching; ν_{as}, asymmetrical stretching; umbrella; ring breathing; ring 1 (C1 to C6), ring 2 (C30 to C37).

Vibrations of MC As to MC (Fig. 1c and d), the main difference between MC and EC is that two methyl groups are attached with nitrogen atoms instead of ethyl groups. Their molecular structures are very similar. Therefore, the vibrational spectra of MC are expected to be like that of EC except for a little difference. Similarly, the C=O stretching of MC at 1671 cm^{-1} also exhibits strong IR absorption intensity (Fig. 5) and weak intensity in Raman spectra (Fig. 4). The MC ring breathing at 1006 cm^{-1} has strong intensity that dominates the Raman spectra in the spectral region from 200 to 2000 cm^{-1} (Fig. 4b). However, they are not observed in IR spectra (Fig. 5). In the low wavenumbers (Fig. 5b), there are two intense IR frequencies at 753 and 696 cm^{-1} that correspond to the C-H and ring out-of-plane bending. They are in an excellent agreement with the simulated IR frequencies except for relative intensity. The frequency at 714 cm^{-1} assigned to the ring C-C-C cissing majorly dominates the

18
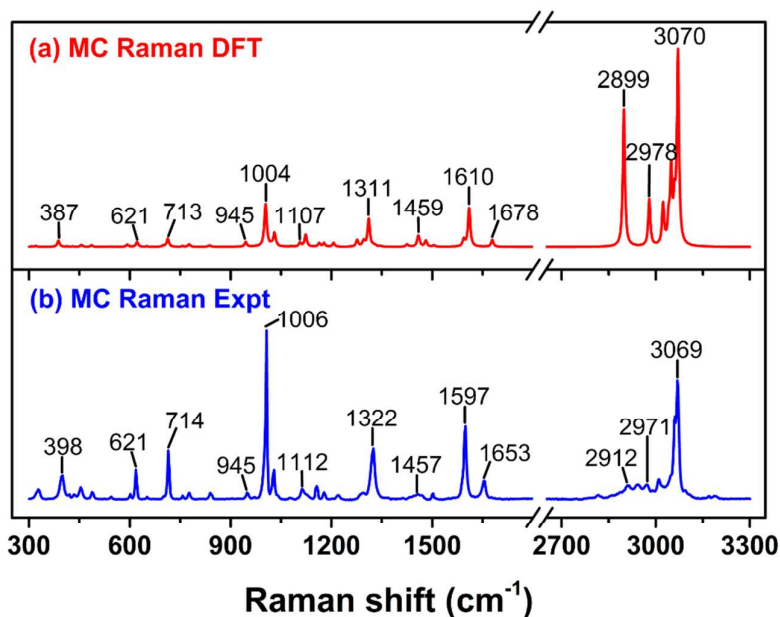
Figure 4 Raman spectra of methyl centralite (N,N'-Dimethyl-N,N'-diphenylurea): (a) theoretical calculation based on DFT and (b) Raman spectrum obtained using 785 nm laser excitation.
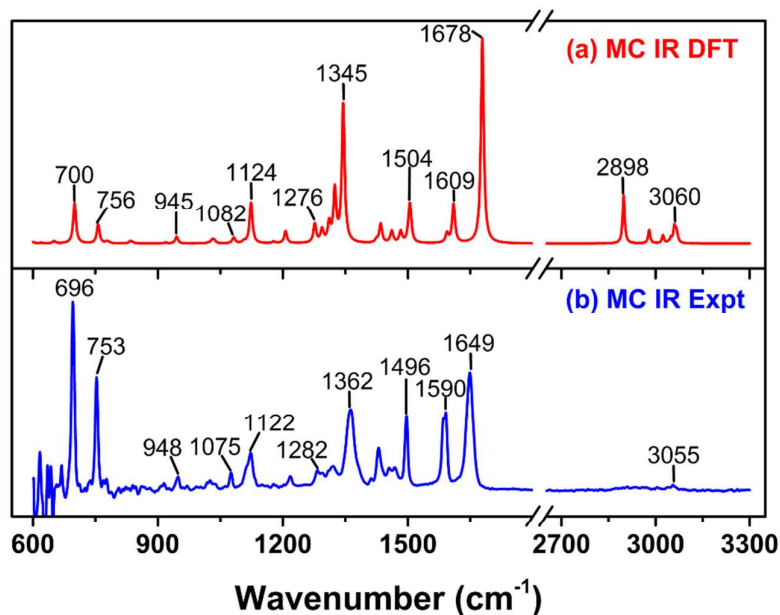
Figure 5 IR spectra of methyl centralite (N,N'-Dimethyl-N,N'-diphenylurea): (a) theoretical calculation based on DFT and (b) IR spectrum obtained using ATR-IR.

low wavenumber region. The C-H stretching modes from 3000 to 3300 are also similar to those of EC.

Compared with the vibrational spectra of EC, there are some missed vibrational modes of ethyl groups in MC, including their C-C stretching, twisting, rocking, and scissoring, as well as wagging modes of -CH_2- in ethyl groups. For examples, in EC vibrational spectra (Fig. 2 and 3), the C13-C16/C23-C26 stretching coupled with the H18-C16-H19/H27-C26-H29 wagging contributes to the frequency at 1078 cm^{-1}, while only ring C-H in-plane bending contributes to the MC frequency at 1077 cm^{-1}. In Raman spectra of EC (Fig. 3), the frequency at 976 cm^{-1} with a moderate intensity could be assigned to the N12-C20-N22 stretching accompanying with the ring 2 breathing and the H14-C13-H15/H24-C23-H25 twisting. However, for MC, this frequency becomes very weak and it is assigned to the ring out-of-plane bending.

The vibrational spectra of MC also shows some differences in the spectral region from 1300 to 1400 cm^{-1}. In Raman spectra (Fig. 4b), the MC C3-N12-C17 and C24-N19-C20 asymmetrical stretching at 1322 cm^{-1} slightly down shifts to ~27 cm^{-1} compared to that of EC at 1349 cm^{-1}. In IR spectra (Fig. 5b), the MC frequency at 1362 cm^{-1} shows a strong intensity, and it also shifts to the low wavenumber compared to the EC frequency at 1397 cm^{-1}. Both of them could be assigned to the N-C-N asymmetrical stretching.

Overall, though the spectra of MC are quite similar to those of EC in both experimental and theoretical results, a few differences were observed. They could be

used to distinguish their Raman and IR spectra. The detail vibrational assignments are

shown in Table 3.

**Table 3** The experimental and calculated IR and Raman spectra of methyl centralite.

Mode	Raman		IR		Assignments
	Expt	DFT	Expt	DFT	
14	327	321			*rock*(N12-C17-N19)
16	398	387			*twist*(N12–C17-N19)
20	454	456			*twist*(N12–C17-N19), βring1, βring2
21	488	486			γ(C17-N12), γ(C17-N19)
22	543	541			γ(C3-N12), γ(C24-N19)
23	592	600			γ(C3-N12), γ(C24-N19), *sciss*(N12–C17-N19)
25	621	618			τ ring1, τ ring2
26	651	652	608	622	β(C17=O18), βring1, βring2
27	698	700	643	648	γring1, γring2
29	715	713	694	700	*ciss*(C1–C6-C5, C2-C3-C4, C25-C24-C26 C27-C31-C29)
30	757	756	752	760	γ(C3-N12, C24-N19), γ((N12–C17-N19)
31	776	777	781	778	γ(C3-N12, C24-N19), γring1, γring2
34	840	837	830	838	γ(C1-H7, C2-H8, C4-H9, C5-H10, C25-H28, C26-H30, C27-H32,C29-H33)
38	949	944	924	927	v_s(N12–C17-N19), ring(1,2) breathing
40	976	974	974	974	γring
44	1006	1004			ring (1,2) breathing
46	1030	1029	1023	1032	v_s(C1-C6-C5, C27-C31-C29)
47			1043	1040	v_s(C1-C6-C5, C27-C31-C29), v_s(C13-N12-C17, C17-C19-C20)
48	1077	1080	1073	1075	β(C-H) in rings
50	1112	1107	1089	1089	*sciss*(N12-C17-C19)
53	1127	1124	1119	1121	*umbrella*(C13-H$_3$, C20-H$_3$), v_{as}(C3-N12-C17, C20-C19-C24)
55	1155	1163	1132	1132	β(C-H in rings)
56	1178	1178	1169	1176	β(C-H in rings)
58	1219	1206	1218	1206	v_{as}(C13-N12-C17, C17-N19-C20)
59	1287	1276	1283	1276	v_{as}(C3-N12-C13, C24-N19-C20)
61	1295	1297	1295	1293	v_{as}(C-C-C) in rings
62	1322	1311	1311	1309	v_{as}(C3-N12-C13, C24-N19-C20), v_s(N12-C17-N19), v(C17=O18)
65	1362	1343	1361	1345	v_{as}(N12-C17-N19)
66	1433	1424	1430	1435	*umbrella*(C13-H$_3$, C20-H$_3$)
70	1457	1459	1454	1461	*sciss*(H14-C13-H15, H21-C20-H23), β(C13-H16, C20-H22,)
72	1470	1481	1469	1482	*sciss* (H14-C13-H16, H22-C20-H23), β (C13-H15, C20-H21,)
75	1500	1504	1496	1504	v(C3-N12, C24-N19), v_s(C2-C3-C4, C1-C6-C5,C25-C24-C26, C27-C31-C29), β(C-H) in rings
76		1594	1585	1594	v_{as}(C2-C3-C4, C1-C6-C5, C25-C24-C26, C27-C31-C29),

					β(C-H) in rings
79	1597	1610	1590	1609	ν(C1-C2, C4-C5, C25-C27, C26-C29), ν(C3-N12, C24-N19), β (C-H) in rings
80	1653	1678	1649	1678	ν(C17=O18), ν$_s$(N12-C17-N19)
82	2912	2899	2910	2899	ν(C13-H14, C13-H15, C13-H16, C20-21, C20-C22, C20-C23)
83	2976	2978	2970	2979	ν(C13-H15, C20-H21), ν$_{as}$(H14-C13-C16, H22-C20-C23)
85	3009	3023	3004	3023	ν$_{as}$(H14-C13-C15, H21-C20-C23)
88	3047	3048	3038	3049	ν(C1-H7, C5-H10, C6-H11, C27-H32, C29-H33, C31-H34)
89	3060	3059	3055	3060	ν(C1-H7, C2-H8, C4-H9, C5-H10, C25-H328, C26-H30, C27-C32, C29-H33)
96	3069	3076	3064	3064	ν(C-H) in rings

Abbreviations: ν, stretching; β, in-plane bending; γ, out-of-plane bending; τ, torsional vibration; sciss, scissoring; rock, rocking; wag, wagging; twist, twisting; ν$_s$, symmetrical stretching; ν$_{as}$, asymmetrical stretching; umbrella; ring breathing; ring1 (C1 to C6), ring2 (C24 to C31).

Raman imaging of centralites

Recently, Lednev and coworkers successfully detected macro and microscopic the inorganic and organic gunshot residue particles collected via "tape lifting" by using FTIR-ATR imaging,[16] which demonstrates great potential in analyzing organic GSR through molecular fingerprinting. Compared to IR imaging, Raman imaging offers better spatial resolution, superb multiplexing capability and a low background.[28] Unfortunately, Raman imaging in detecting the gunshot residues is little explored. Herein, we applied Raman imaging to detect centralites particles on coverslips. We recorded Raman data of EC and MC using the home-built LSRM with ~0.7 μm spatial resolution and an integration time of 10 sec per scan step. Figure 6a and b show the bright-field image of the mapped area (left) and the corresponding the corresponding Raman maps (right) for EC and MC, respectively. Both Raman maps were generated by the strong peak intensity at 1006 cm^{-1} that is assigned to the ring breathing for EC and MC. The skyblue, yellow and red colored pixels (Fig. 6a and b)
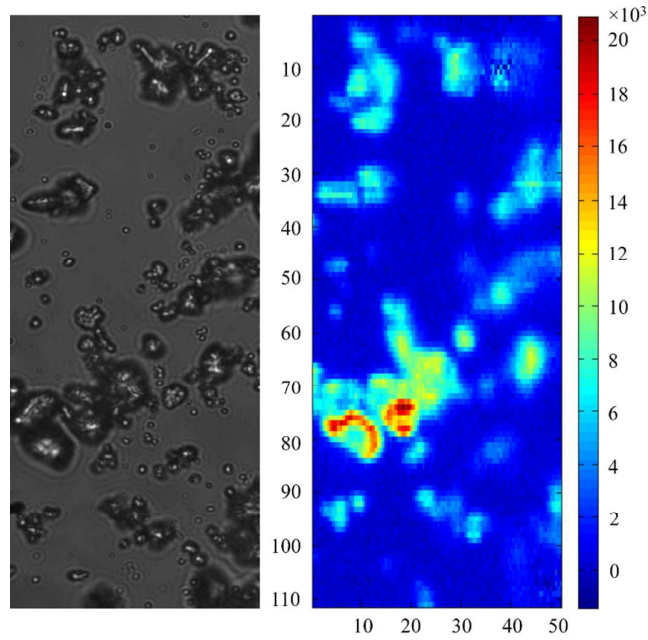
(a) EC
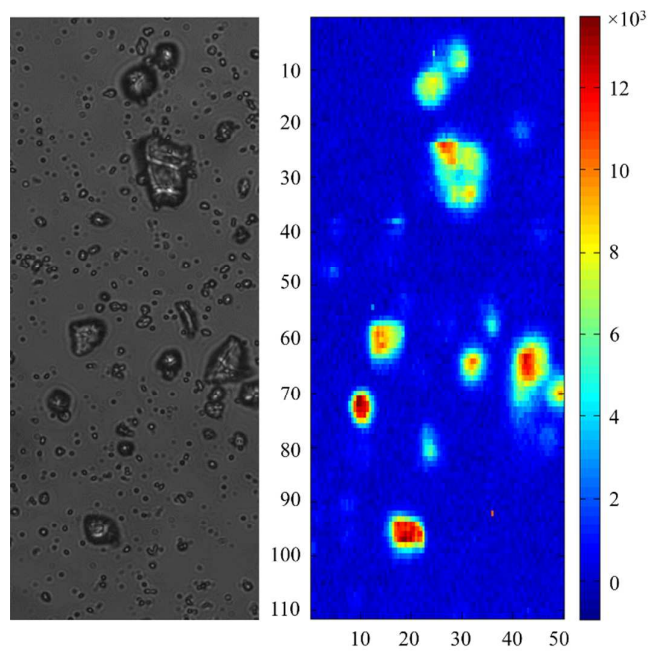
(b) MC

Figure 6 Raman imaging for detection of centralites: (a) and (b) are the visual image

of the mapped area (left) and its corresponding Raman maps (right) for EC and MC

23

powder particles on coverslips, respectively. The pixels are color coded using the

intensity of 1006 cm^{-1}. The x and y axis units are in μm.

represent the detection of EC and MC particles. The detected particle sizes are

estimated to be from 2 to 13 μm. Overall, the Raman maps of EC and MC match the

bright-field optical images well. Therefore, LSRM can be a rapid analytical

instrument for analyzing centralites.

The present vibrational frequency study of centralites based on DFT simulation is

a significant step for vibrational analysis and imaging of organic gunshot residues at

the molecular level based on their fingerprint characteristics. It will be of interest to

further explore trace amount detection of organic gunshot residues by

surface-enhanced Raman scattering (SERS) based on monolithic nanoporous gold

disks with large specific surface area and high density, internal plasmonic

hot-spots.[29-32] Thus, Raman imaging for real gunshot residue samples based on SERS

could be further developed. In addition, our results can be combined with recently

high-speed Raman imaging systems by active-illumination to provide higher

throughput for practical applications.[33, 34] Efforts in this direction are proceeding in

our laboratories.

Conclusions

In this paper, the molecular structures and vibrational landscapes of ethyl and

methyl centralites were investigated by DFT level employing the 6-311++g(df,pd)

basis set. Since vibrational spectroscopy has emerged as a viable technique in analyzing organic GSR, the DFT-based landscaping provides essential information for centralites for the first time. It will help to advance our understanding of centralite structures, and is of significance for further vibrational studies in organic GSR detection such as FT-ATR imaging, SERS and Raman imaging. Overall, the simulated vibrational frequencies are in a good agreement with the experimental results. Though MC exhibits a structure very similar to EC, a few differences were observed in both theoretical and experimental results. Both Raman and IR frequencies of EC and MC are comprehensively assigned according to the simulated results. The Raman mapping of EC and MC based on high-throughput line-scan Raman microscopy represents the first attempt to produce rapid and effective analysis. The vibrational imaging will grow into an important analytical technique in organic GSR detection.

Acknowledgement

References

1. M. Trimpe, in *FBI Law Enforcement Bulletin*, 2011, vol. May.

2. H. Meng and B. Caddy, *Journal of forensic sciences*, 1997, **42**, 553-570.

3. F. Saverio Romolo and P. Margot, *Forensic Science International*, 2001, **119**, 195-211.

4. O. Dalby, D. Butler and J. W. Birkett, *Journal of forensic sciences*, 2010, **55**, 924-943.

5. J. Bueno, V. Sikirzhytski and I. K. Lednev, *Analytical chemistry*, 2012, **84**, 4334-4339.

6. J. Bueno, V. Sikirzhytski and I. K. Lednev, *Analytical Chemistry*, 2013, **85**, 7287–7294.

7. J. J. Perez, P. M. Flanigan, J. J. Brady and R. J. Levis, *Analytical Chemistry*, 2012, **85**, 296-302.

8. D. Laza, B. Nys, J. D. Kinder, K. D. Mesmaeker and C. Moucheron, *Journal of forensic sciences*, 2007, **52**, 842-850.

9. H.-h. Meng and B. Caddy, *Analyst*, 1995, **120**, 1759-1762.

10. H. Meng and B. Caddy, *Journal of forensic sciences*, 1996, **41**, 213-220.

11. H. Meng and B. Caddy, *Journal of Forensic Sciences*, 1994, **39**, 1215-1215.

12. M. Zhao, S. Zhang, C. Yang, Y. Xu, Y. Wen, L. Sun and X. Zhang, *Journal of Forensic Sciences*, 2008, **53**, 807-811.

13. M. López-López, J. J. Delgado and C. García-Ruiz, *Analytical Chemistry*, 2012, **84**, 3581-3585.

14. M. López-López, J. L. Ferrando and C. García-Ruiz, *Analytica Chimica Acta*, 2012, **717**, 92-99.

15. J. Bueno and I. K. Lednev, *Analytical Methods*, 2013, **5**, 6292-6296.

16. J. Bueno and I. K. Lednev, *Analytical Chemistry*, 2014, **86**, 3389–3396.

17. D. S. Sholl and J. A. Steckel, in *Density Functional Theory*, John Wiley & Sons, Inc., 2009, pp. 113-130.

18. J. Qi and W.-C. Shih, *Applied Optics*, 2014, **Accepted**.

19. M. J. Frisch, G. W. Trucks and H. B. Schlegel et al., GAUSSIAN 09, Revision A.01, Gaussian Inc., Wallingford, CT, **2009**.

20. A. D. Becke, *Physical Review A*, 1988, **38**, 3098.

21. A. D. Becke, *The Journal of Chemical Physics*, 1993, **98**, 5648.

22. J. Baker, A. A. Jarzecki and P. Pulay, *The Journal of Physical Chemistry A*, 1998, **102**, 1412-1424.

23. D. Lin-Vien, N. B. Colthup, W. G. Fateley and J. G. Grasselli, *The handbook of infrared and Raman characteristic frequencies of organic molecules*, Academic Press, 1991.

24. H. M. Badawi and W. Förner, *Spectrochimica Acta Part A: Molecular and Biomolecular Spectroscopy*, 2012, **95**, 435-441.

25. J. D. Louden, J. Kelly and J. Phillipson, *Journal of Raman Spectroscopy*, 1987, **18**, 137-140.

26. P. M. Wojciechowski, W. Zierkiewicz, D. Michalska and P. Hobza, *The Journal of chemical physics*, 2003, **118**, 10900-10911.

27.   C. M. Ramos, L. F. Alzate, N. M. Hernández, S. P. Hernández and N. Mina, *Journal of Molecular Structure: THEOCHEM*, 2006, **769**, 69-76.

28.   Y. Zhang, H. Hong and W. Cai, *Current pharmaceutical biotechnology*, 2010, **11**, 654.

29.   M. Li, J. Lu, J. Qi, F. Zhao, J. Zeng, J. C.-C. Yu and W.-C. Shih, *Journal of Biomedical Optics*, 2014, **19**, 050501-050501.

30.   J. Qi, P. Motwani, M. Gheewala, C. Brennan, J. C. Wolfe and W.-C. Shih, *Nanoscale*, 2013, **5**, 4105-4109.

31.   G. M. Santos, F. S. Zhao, J. B. Zeng and W. C. Shih, *Nanoscale*, 2014, **6**, 5718-5724.

32.   F. Zhao, J. Zeng, M. M. P. Arnob, P. Sun, J. Qi, P. Motwani, M. Gheewala, C.-H. Li, U. Strych, A. Paterson, B. Raja, R. Willson, J. C. Wolfe, T. R. Lee and W.-C. Shih, *Nanoscale*, 2014.

33.   J. Qi and W.-C. Shih, *Opt. Lett.*, 2012, **37**, 1289-1291.

34.   J. Qi, J. Li and W.-C. Shih, *Biomed. Opt. Express*, 2013, **4**, 2376-2382.

TOC figure